Water Droplet Impingement on Airfoils and Aircraft Engine Inlets for Icing Analysis

Michael Papadakis*
Wichita State University, Wichita, Kansas 67208
and
R. Elangovan,† George A. Freund Jr.,‡ and Marlin D. Breer§
Boeing Military Airplanes, Wichita, Kansas

This paper includes the results of a significant research program for verification of computer trajectory codes used in aircraft icing analysis. Experimental water droplet impingement data have been obtained in the NASA Lewis Research Center Icing Research Tunnel for a wide range of aircraft geometries and test conditions. The body whose impingement characteristics are required is covered at strategic locations by thin strips of moisture absorbing (blotter) paper and then exposed to an airstream containing a dyed-water spray cloud. Water droplet impingement data are extracted from the dyed blotter strips by measuring the optical reflectance of the dye deposit on the strips with an automated reflectometer. Impingement characteristics for all test geometries have also been calculated using two recently developed trajectory computer codes. Good agreement is obtained with experimental data. The experimental and analytical data show that maximum impingement efficiency and impingement limits increase with mean volumetric diameter for all geometries tested. For all inlet geometries tested, as the inlet mass flow is reduced, the maximum impingement efficiency is reduced and the location of the maximum impingement shifts toward the inlet inner cowl.

Nomenclature

D = droplet diameter, μm
$D(\mathrm{I})$ = diameter of droplets in group I for a discrete distribution, μm
M = Mach number of air flow at freestream
n = number of droplet groups available in a discrete droplet distribution
s = surface distance from reference point, cm
V_∞ = freestream velocity, mph
W = engine inlet mass flow, lbm/s
α = angle of attack, deg
β = local impingement efficiency for clouds with uniform droplet size
$\bar{\beta}$ = local impingement efficiency for clouds with nonuniform droplet size
θ = circumferential location for inlets, deg
ρ_w = density of water, g/cm^3

I. Introduction

AIRCRAFT flying at subsonic speeds through clouds below about 8000 m can be subject to ice formation on critical aerodynamic surfaces. Ice accretion results from very small supercooled droplets, usually 5–50 μm in diameter, which can freeze on impact with the aircraft surface. The local and total rates of droplet impingement as well as the extent of the impingement are important design considerations for aircraft ice protection systems.

In recent years, a number of analytical codes[1–3] capable of predicting the impingement characteristics of two- and three-dimensional bodies have been developed. These analytical tools are used by industry to assist in the design and certification of de-icing and anti-icing systems.

Application of these computer codes to icing analysis requires extensive validation against experimental data. In the past, trajectory codes have been evaluated by comparison with experimental data generated by NACA in the 1950s.[4–7] These experimental data, however, were limited to low-speed studies of airfoil sections of interest to the aviation community in the 1940–1955 time period and to simple axisymmetric geometries. No experimental water droplet impingement data are available for modern airfoil sections. In addition, almost no experimental impingement data exist for aircraft engine inlets.

Aircraft engine inlets have highly three-dimensional flows. Trajectory codes used in predicting the impingement characteristics of inlet configurations must be extensively validated against experimental data obtained for such geometric flow conditions.

This paper presents experimental water droplet trajectory obtained for a NACA 65_2015 airfoil, a modern supercritical airfoil, an axisymmetric inlet, and a Boeing 737-300 inlet. Both inlets are representative of modern aircraft inlet geometries. Impingement data for the stated geometries are presented for a wide range of test conditions.

The experimental method used for the present testing is similar to that employed by NACA in the 1950s. The main difference is in the data reduction method used to determine distribution of the dye deposit on blotter strips and, hence, the local impingement efficiency. In addition, a different method was used to determine the liquid water content (LWC). This paper gives brief descriptions of the experimental and data reduction methods. Detailed descriptions of these methods can be found in Ref. 8.

Results from two computer trajectory codes are also presented here. One of these codes can be applied to two-dimensional and axisymmetric flows,[9] whereas the other can predict the impingement characteristics of complex three-dimensional configurations such as engine inlets at angle of attack.[10] The analytical impingement data are in good agreement with the experimental data.

Presented in part as AIAA Paper 86-0406 at the AIAA 24th Aerospace Sciences Meeting, Reno, NV, Jan. 6-9, 1986; received Oct. 29, 1988; revision received Jan. 29, 1990. Copyright © 1990 by the American Institute of Aeronautics and Astronautics, Inc. All rights reserved.

*Assistant Professor, Aerospace Engineering Department. Member AIAA.
†Senior Specialist Engineer, Advanced Concepts Staff. Member AIAA.
‡Senior Specialist Engineer, Low Observable Technology Group.
§Engineer Supervisor, Mechanical Systems. Member AIAA.

II. Test Description

Experimental Setup

The experimental method involves use of a special dye material dissolved in distilled water. Concentration of the solution is known in advance. Water droplets produced by a specially designed spray system installed in the icing research tunnel (IRT) are collected on blotter paper fixed in thin strips to the model surface of interest.

To determine the local LWC in the freestream spray cloud, a "reference collector mechanism"[8] was used. After testing a given model, the collector was positioned close to the location where the model had been installed and was exposed to the spray cloud under identical tunnel conditions as the model itself. Spraying times of various lengths, usually in the range of 0.5–3 s, were used to calibrate the collector. A rectangular blotter strip (0.2 × 1.5 in.) mounted on the collector mechanism was used to collect dye during each spray.

The true 100% efficiency for the collector is determined by correcting the measured impingement efficiency.[8] The local impingement efficiency $\bar{\beta}$ for the model is then determined as follows:

$$\text{Local impingement efficiency } \bar{\beta} \text{ of model at a given location} = \frac{\text{Measured dye mass per unit area on model at a given location}}{\text{Dye mass per unit area for true 100\% impingement efficiency}}$$

Airfoil Configurations

The airfoils tested include a NACA 65_2015 section and a MS(1)-0317 supercritical section. Figure 1 shows the NACA 65_2015 airfoil with blotter strips installed at two spanwise locations. Impingement data were obtained for two angles of attack and two droplet sizes. All tests were conducted at an airspeed of approximately 175 mph and a tunnel air temperature of approximately 50°F.

Inlet Configurations

Two inlet geometries were tested: an axisymmetric inlet and a Boeing 737-300 inlet. Tests for these inlets were conducted at two different mass flows, two angles of attack, and two mean volumetric diameters (MVDs). In addition, the Boeing 737-300 inlet was tested at a third mass flow setting for one MVD size and one angle of attack. The airspeed for all inlet tests was approximately 165 mph. The inlet mass flow was varied by adjusting the regulating valve in the NASA IRT suction flow pipe. The engine inlet was connected to the NASA suction system by means of a flexible duct to permit variations in the inlet angle of attack.

Accurate mass flow measurements for inlet tests are essential for comparing analytical and experimental aerodynamic and impingement data. To measure the suction mass flow, a temperature compensated velocity probe was installed in the 24-in. i.d. suction pipe in the NASA suction system. This probe was calibrated utilizing a precalibrated 16-ft long, 8-in. i.d. duct with pitot tube, wall static tap, and thermocouple installed.

The sensor has a logarithmic response that allows for accurate measurements of airflow velocities as low as 0.17 ft/s. An electronic control box connected to the probe output was used to linearize the nonlinear signal of the probe.

Inlet Pressure Survey

When comparing experimental and analytical water droplet trajectory data, it is important to verify that the experimental and analytical flowfields are in good agreement. Prior to acquiring droplet impingement data for the two inlet models, surface pressure distributions for both inlets were measured using existing model wall static taps. The NASA Lewis Research Center IRT automated data acquisition system was used to record the required pressure data. Identical tunnel conditions were used for the aerodynamic and impingement tests. Experimental and analytical surface pressure data are presented in terms of surface Mach number in this paper and show very good agreement.

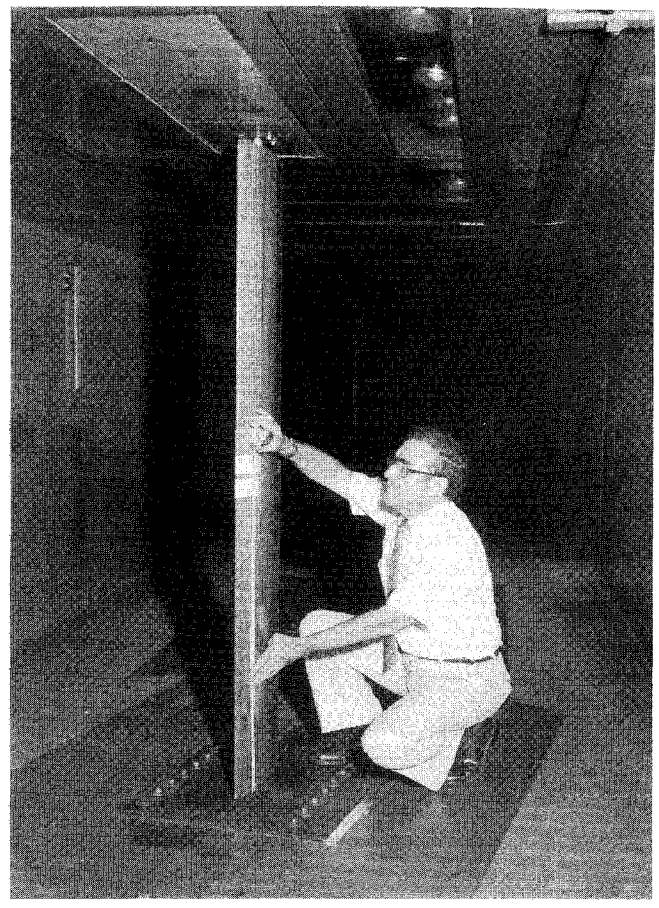

Fig. 1 NACA 65_2015 airfoil installed in NASA IRT.

Inlet Droplet Impingement

Blotter strips typically 1.5 in. wide and of various lengths, depending on the inlet being tested, were attached to the inner and outer surfaces of the inlet at specified circumferential locations (θ). The length of each strip was selected to include the area of water impingement. Once the tunnel conditions were set and the inlet mass flow was adjusted to give the required inlet capture area ratio, the spray system was activated and a dye deposit was obtained on the blotters. Figure 2 shows the axisymmetric engine inlet with blotter strips attached.

Test Condition Matrix

Models tested and test conditions are shown in Table 1. The tests produced a total of 504 blotter strips. These strips were analyzed by scanning along the length of each strip at three different width locations using the automated data processing system discussed in Sec. IV.

A variety of test models and conditions were selected to provide an extensive data base. Angles of attack for both airfoil sections were limited to 8 deg to avoid flow separation. Engine inlet angle of attack was limited to 15 deg to remain within the uniform region of the tunnel spray cloud.

Spray pressure ratios chosen (0.8 and 0.65) correspond to water droplet clouds with MVDs of approximately 16 and 20 μm, which are representative of icing cloud conditions. Engine inlet mass flows of 22.9, 17.2, and 11.5 lbm/s correspond to capture area ratios of 1, 0.75, and 0.5, respectively,

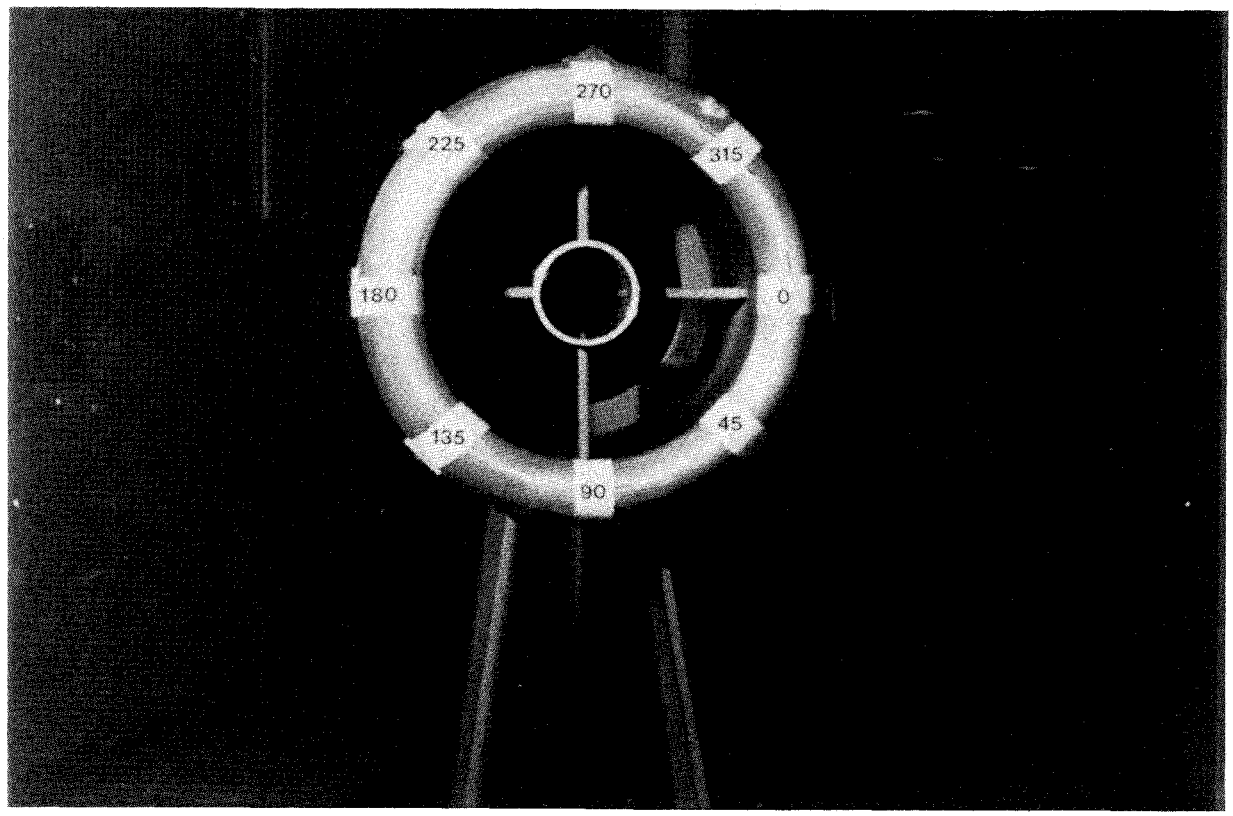

Fig. 2 Blotter strip locations for axisymmetric inlet.

for the 1/4 scale models at the tunnel speed of 165 mph. These capture area ratios are representative of icing design flight conditions. Each set of test conditions was repeated three times to obtain a statistical average.

The single blade reference collector was calibrated using six different exposure times, two positions (corresponding to model blotter strip positions), and two droplet sizes giving a total of 24 tests. This collector was used to determine the cloud liquid water content for the two-dimensional test models. The four-blade reference collector was calibrated using two exposure times, two positions, two droplet sizes, and three repeats giving a total of 24 tests. The results obtained from the four-blade collector were used to determine the cloud liquid water content for the engine inlet models.

Table 1 Test condition matrix

Model Description	Angle of attack, deg	Suction flow, lbm/sec	Spray system pressure ratio, P_{air}/P_{H_2O} MVD 16 μm	MVD 20 μm
65_2015 airfoil	0, 8	—	0.65	0.80
MS(1)-0317 supercritical airfoil	0, 8	—	0.65	0.80
Axisymmetric engine inlet	0, 15	17.2, 22.9	0.65	0.80
737-300 engine inlet	0, 15	17.2, 22.9	0.65	0.80
737-300 engine inlet	15	11.5	—	0.80
Reference collector (single blade)	0	—	0.65	0.80
Reference collector (four blades)	0	—	0.65	0.80

III. Droplet Size and Distribution

Droplet trajectory computer codes can be validated by comparing calculated impingement efficiency with experimentally determined efficiency. The impingement efficiency calculation requires knowledge of spray cloud droplet size distribution and MVD. The MVD is that diameter for which half of the total liquid water content is contained in droplets larger than the mean and half in droplets smaller than the mean. Knowing the droplet size distributions, MVD can be calculated as follows.

If $n(D)$ is the number of particles per unit sampling volume having diameters between D and $D + dD$ (volumes between V and $V + dV$) then D_{MVD} can be calculated from

$$\frac{\frac{\pi}{2}\rho_w \int_{D_{min}}^{D_{MVD}} n(x)x^2\,dx}{\frac{\pi}{2}\rho_w \int_{D_{min}}^{D_{max}} n(x)x^2\,dx} = 0.5 \tag{1}$$

If the particle number density is given in N discrete groups such that $n_i(D_i)$ is the number of particles in group i having diameters between D and $D + dD$, then Eq. (1) can be written as

$$\frac{\frac{\pi}{6}\rho_w \sum_{i=1}^{K} n_i(D_i)D_i^3}{\frac{\pi}{6}\rho_w \sum_{i=1}^{N} n_i(D_i)D_i^3} \tag{2}$$

where $D_K = D_{MVD}$.

Industry practice generally has been to accept Langmuir D distribution as the proper droplet size distribution and to utilize it in computer codes. The Langmuir distribution was arrived at from measurements made on the summit of Mt. Washington.[11] Measurements of the rate of deposition of ice

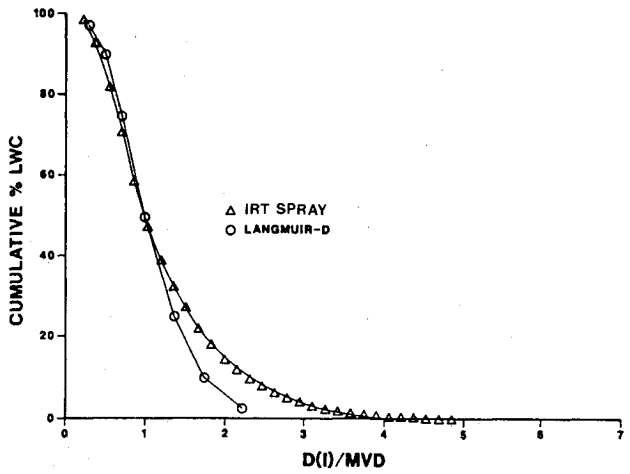

Fig. 3 Measured and Langmuir D cumulative droplet distributions for MVD = 20 μm.

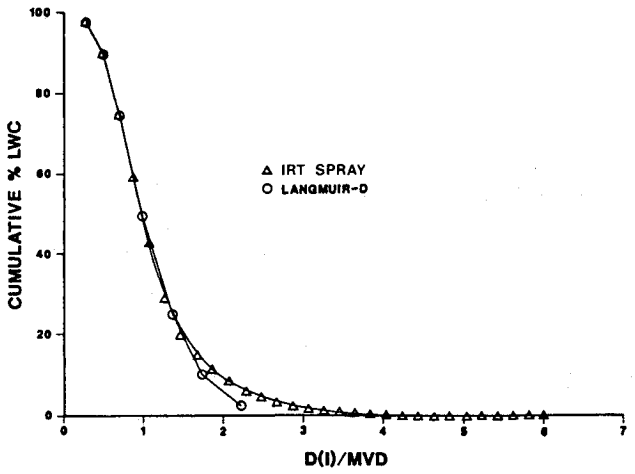

Fig. 4 Measured and Langmuir D cumulative droplet distributions for MVD = 16 μm.

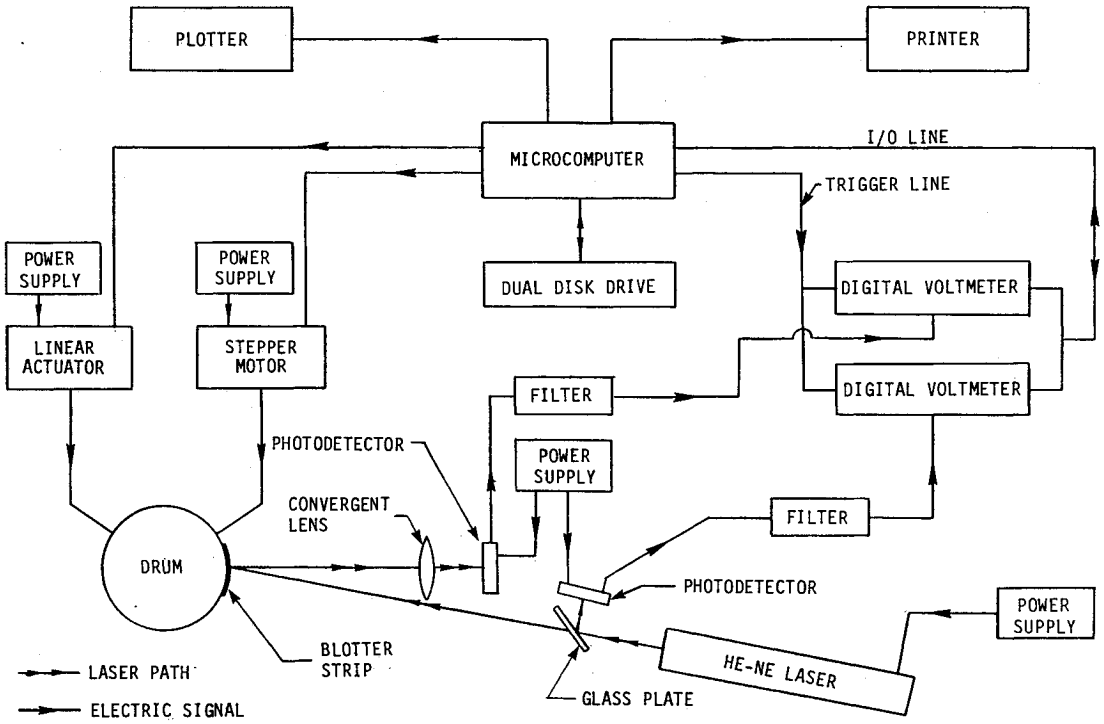

Fig. 5 Schematic of automated reflectometer and digital data acquisition system.

on slowly rotating cylinders exposed to supercooled clouds blowing over the summit were matched with that of the theoretical calculations. This trial and error procedure produced Langmuir distribution. To verify the applicability of Langmuir D distribution to the IRT, nozzle spray cloud measurements were performed using a laser particle sizing instrument. The composite cloud distributions determined by these measurements are shown in Figs. 3 and 4. The corresponding Langmuir D distributions are also shown in these figures for comparison. The agreement between the Langmuir D and the actual distributions is very good.

IV. Impingement Data Reduction

In the present dye-tracer technique, the spatial variations in the concentration of the dye along the length of the blotter are determined by reflectance spectroscopy. The reflectance method is based on the assumption that the surface reflectance of the paper is a measure of the dye mass per unit area on the paper. Knowledge of the dye concentration in the spray water then gives water impingement rate.

The blotter paper strips are illuminated with light from a He-Ne laser. Light diffusely reflected from the paper is collected by a lens and focused onto a silicon photodetector. The voltage from the silicon photodetector decreases as light is absorbed by the dye; the amount of absorption is related to the concentration of the dye deposited on the paper. An automated reflectometer with a digital data acquisition system was developed to extract the raw data from the blotter paper strips, to calculate the impingement efficiency curves, and to print and plot the results. A schematic of the automated reflectometer and digital data acquisition system is shown in Fig. 5.

Laser Reflectometer

A horizontally rotating drum was used for the mounting and positioning of blotter paper. This allowed the blotter paper strips to be accurately and reproducibly positioned. Rotation of the drum is controlled by a stepper motor capable of 800 steps/revolution. Since the drum radius is 68.26 mm (2.688 in.), this corresponds to a movement of 0.54 mm (0.021 in.)/step. Vertical motion of the drum is controlled by

a linear actuator that moves the drum in 0.0254-mm (0.001-in.) increments.

Optical feedback is accomplished by splitting off a portion of the incident laser beam near the beam port of the laser with a glass plate at an angle of approximately 45 deg. This splitoff beam is monitored by a silicon photodiode operating in a photoconductive mode. Light reflected from the blotter paper is also monitored by a silicon photodiode. The signal from the photodiodes is input to separate amplifier circuits with gains of 500 : 1 on the signal and 10 : 1 on the feedback. Filtering of high-frequency electrical noise is also provided by the amplifier circuitry. This ensures that electrical noise, comparable in magnitude to the signal, is not a problem. Voltages from the detectors are ratioed by the data acquisition system to take into account any drift in the laser output power that may occur over a period of hours. The laser used has a polarized output so as to reduce fluctuations in the laser output power.

The complete optical and mechanical system, with associated electronics and power supplies, is mounted on aluminum plates in a two-tiered structure. Tests conducted with this system indicate that the instrument itself will measure reproducibly to $\pm 0.3\%$. The largest uncertainty in extracting data from an individual strip comes from the blotter paper itself, whose reflectance varies about $\pm 1.0\%$, in addition to the instrumental uncertainty.

Digitial Data Acquisition System

The data acqusition system consists of a Hewlett-Packard HP-85 desk top computer, disk drive, printer, and two digital voltmeters. Software was developed to extract data from the blotter paper strips, to store this raw data in files, to process the data into impingement efficiencies, and to print and plot the efficiency data.

Figure 6 shows the various stages of the digital data reduction process. The results shown are for the NACA 65_2015 airfoil section at $\alpha = 0$ deg. The average values of reflectivity, dye mass (μg/cm^2), and impingement efficiency are plotted vs surface distance measured from the highlight mark. At the point where reflectivity is minimum, the dye mass and impingement efficiency reach their maximum values. The maximum value of impingement efficiency for this test model at $\alpha = 0$ deg corresponds to the highlight location. The highlight, however, cannot always be marked accurately on the blotter paper. This can result in the $\bar{\beta}$ curve being slightly shifted with respect to the highlight location.

V. Results and Discussion

Experimental and analytical impingement efficiency data for the models and test configurations of Table 1 are presented in this section. The standard method for presenting droplet impingement trajectory results is to plot local impingement efficiency reach their maximum values. The main features of these plots are 1) the overall shape of the $\bar{\beta}$ curve, 2) the location and magnitude of the peak efficiency, and 3) the extent of the curve tails (impingement limits).

All analytical curves have been obtained by using the measured composite water droplet distributions presented in Figs. 3 and 4.

Experimental aerodynamic data and analysis results are also presented for one of the inlet models.

Aerodynamic Data

Aerodynamic data were obtained for both inlets for all test configurations. Comparison of experimental and analytical impingement data requires that analytical and experimental flowfields be in good agreement. Analytical flowfields were generated using the computer codes discussed in Refs. 12–14. These codes solve the full partial differential equations for compressible transonic flow using a finite difference scheme. Experimental and computational results of surface Mach numbers for the axisymmetric inlet are shown in Fig. 7. In this figure, the axial distance X is measured from the leading edge of the inlet. Good correlation between test and analysis is demonstrated.

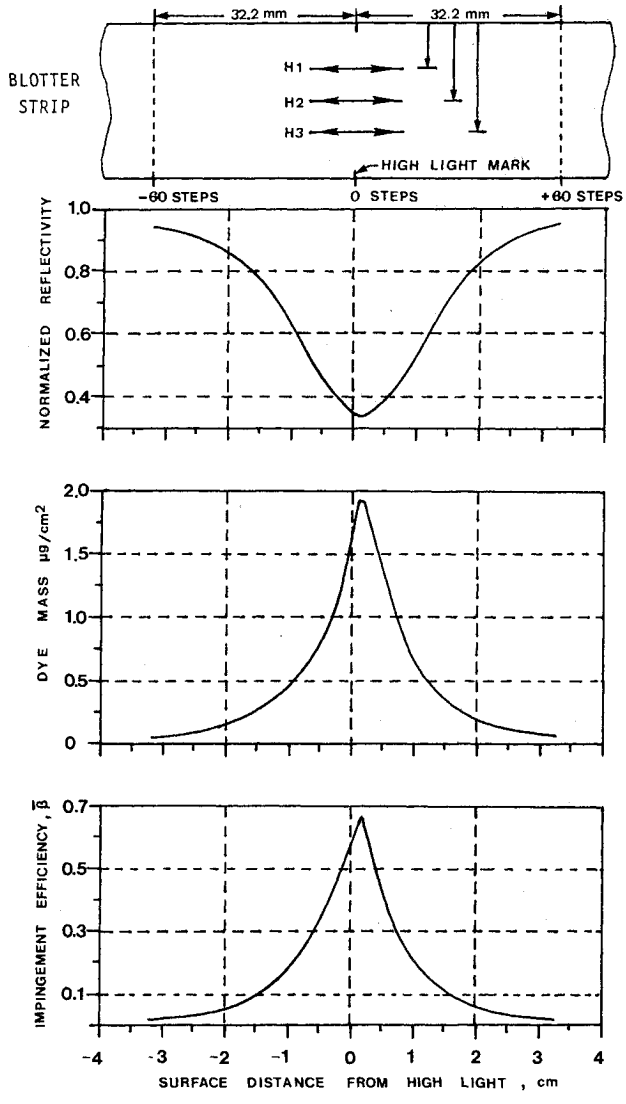

Fig. 6 Plot of average output data vs surface distance.

Impingement Data

Two-Dimensional Flow

For both airfoils, blotter strips were positioned at two spanwise locations, as shown in Fig. 1, and each test condition (i.e., α, MVD) was repeated three times. A total of six blotter strips were obtained for each combination of α and MVD, giving six $\bar{\beta}$ curves. Since the flow is two dimensional, these six curves can be averaged to give a single $\bar{\beta}$ curve. Averaged $\bar{\beta}$ curves for both airfoils are shown in Fig. 8.

For the case of symmetric airflow about the model, symmetric distributions are observed, as expected. For airfoils at 8 deg angle of attack, test data show that the shift in $\bar{\beta}_{max}$ position results from the shift in flow stagnation point, and the increase in water collected is due to the greater frontal projected area. For both airfoils at $\alpha = 0$ deg, the analytical impingement efficiency curves agree well with the test data and show similar trends. For both airfoils at $\alpha = 8$ deg, the agreement between analytical and test data is observed to be fair. The discrepancy between experimental and analysis data for the $\alpha = 8$ deg case is attributed to tunnel wall and model blockage effects. Analytical results presented do not take into account these effects.

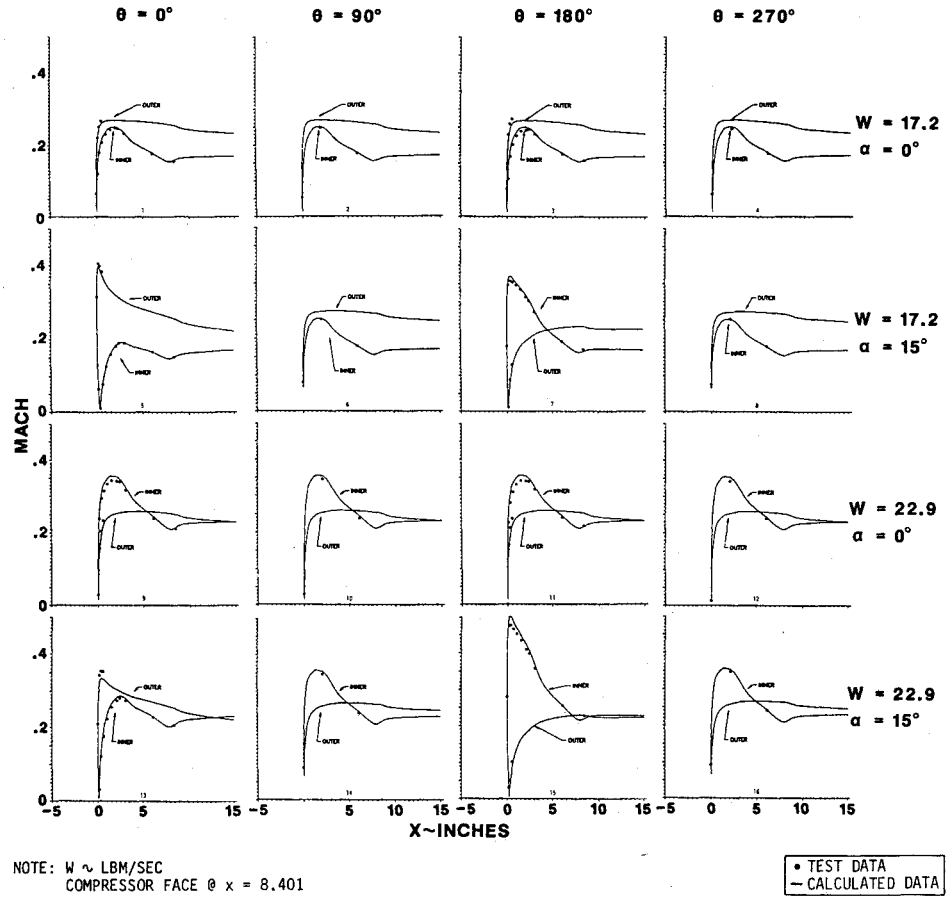

Fig. 7 Axisymmetric engine inlet aerodynamic performance comparison, $V_\infty = 165$ mph.

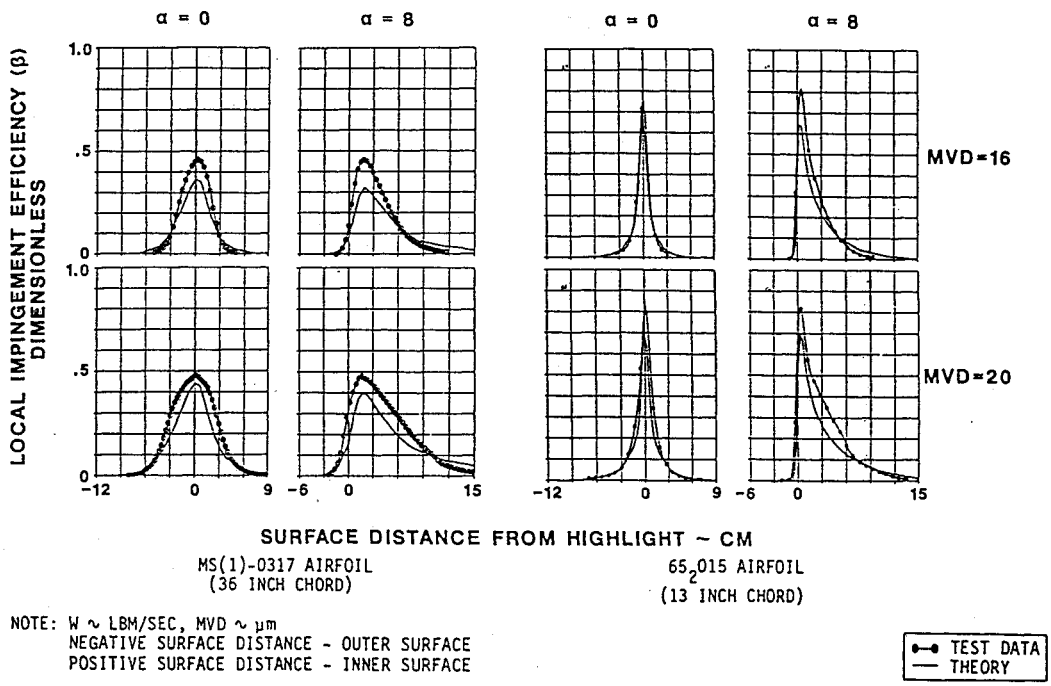

Fig. 8 Impingement efficiency—test and theory for 65_2015 and MS(1)-0317 airfoils, $V_\infty = 175$ mph.

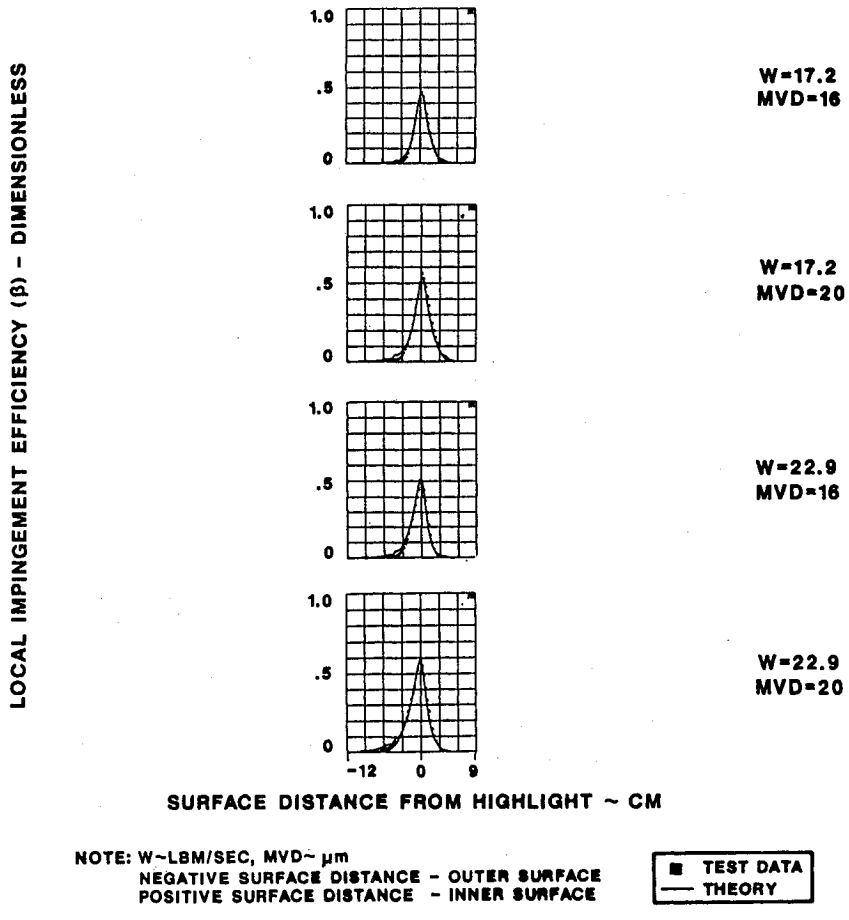

Fig. 9 Impingement efficiency—test and theory for axisymmetric inlet $\alpha = 0$ deg, $V_\infty = 165$ mph.

Axisymmetric Flow

Impingement efficiency results for the axisymmetric inlet at 0 deg angle of attack are presented in Fig. 9. The results shown for each test configuration are the average of 12 $\bar{\beta}$ curves obtained from 12 blotter strips (three runs, four circumferential locations per run). Agreement between test and analysis is good for all test configurations. The following trends are observed:

1) For the same inlet mass flow, decreasing the MVD of the cloud reduces both $\bar{\beta}_{max}$ and impingement limits.

2) For the same cloud MVD, reducing the inlet suction flow reduces the value of $\bar{\beta}_{max}$ and shifts the peak location toward the inner cowl. No change in the extent of the impingement limits ($s_{max} - s_{min}$) is observed. However, both impingement limits shift slightly toward the inside of the inlet.

3) For the high mass flow (capture area ratio = 1), the peak location is at the highlight.

4) Maximum $\bar{\beta}_{max}$ is approximately 58% and corresponds to MVD = 20 μm and inlet mass flow = 22.9 lbm/s. Minimum $\bar{\beta}_{max}$ is approximately 47% and corresponds to MVD = 16 μm and inlet mass flow = 17.2 lbm/s.

Three-Dimensional Flow

Impingement data for the axisymmetric inlet at $\alpha = 15$ deg and for the Boeing 737-300 inlet at $\alpha = 0$ and 15 deg are presented in this section. The Boeing inlet has a three-dimensional geometry; therefore, the flowfield is three dimensional for both angles of attack.

Impingement data are plotted for a number of circumferential locations. These locations are represented by the variable θ. The engine inlet upper lip corresponds to $\theta = 0$ deg, whereas the engine inlet lower lip corresponds to $\theta = 180$ deg. Both engine inlets were mounted in the tunnel so that the plane containing the inlet axis and the locations $\theta = 0$ and 180 deg was parallel to the tunnel floor. This plane is called the plane of symmetry, hereon. Change in angle of attack was obtained by rotating the inlets about an axis perpendicular to the plane of symmetry. Therefore, inlet geometry and flow conditions are symmetric with respect to this plane. Circumferential locations $\theta = 45$, 90, and 135 deg are below the plane of symmetry, whereas locations $\theta = 225$, 270, and 315 deg are above this plane.

The single experimental $\bar{\beta}$ curves presented for the axisymmetric and 737-300 inlets have been obtained by averaging the data obtained from three test runs. The blotter strips used to produce the averaged $\bar{\beta}$ curves for each θ location are the following: $\theta = 0$ deg—three blotter strips from location $\theta = 0$ deg; $\theta = 45$ deg—six blotter strips, three from location $\theta = 45$ deg and three from location $\theta = 315$ deg; $\theta = 90$ deg—six blotter strips, three from location $\theta = 90$ deg and three from location $\theta = 270$ deg; $\theta = 135$ deg—six blotter strips, three from location $\theta = 135$ deg and three from location $\theta = 225$ deg; and $\theta = 180$ deg—three blotter strips from location $\theta = 180$ deg.

Impingement efficiency data for the axisymmetric inlet at 15 deg angle of attack for two inlet mass flows, two cloud MVDs and five different circumferential locations ($\theta = 0$, 45, 90, 135, and 180 deg) are presented in Fig. 10.

Overall, good agreement between test and analysis is demonstrated for the majority of test configurations and inlet locations. The only noticeable disagreement occurs at $\theta = 0$ deg for all test configurations. The reason for this discrepancy is not clear but cloud uniformity is a factor under consideration. Future tests will help resolve this problem.

The following trends are seen for the axisymmetric inlet at 15-deg angle of attack.

1) For the same inlet mass flow and surface location, the larger the MVD of the cloud, the greater the values of $\bar{\beta}_{max}$ and the impingement limits.

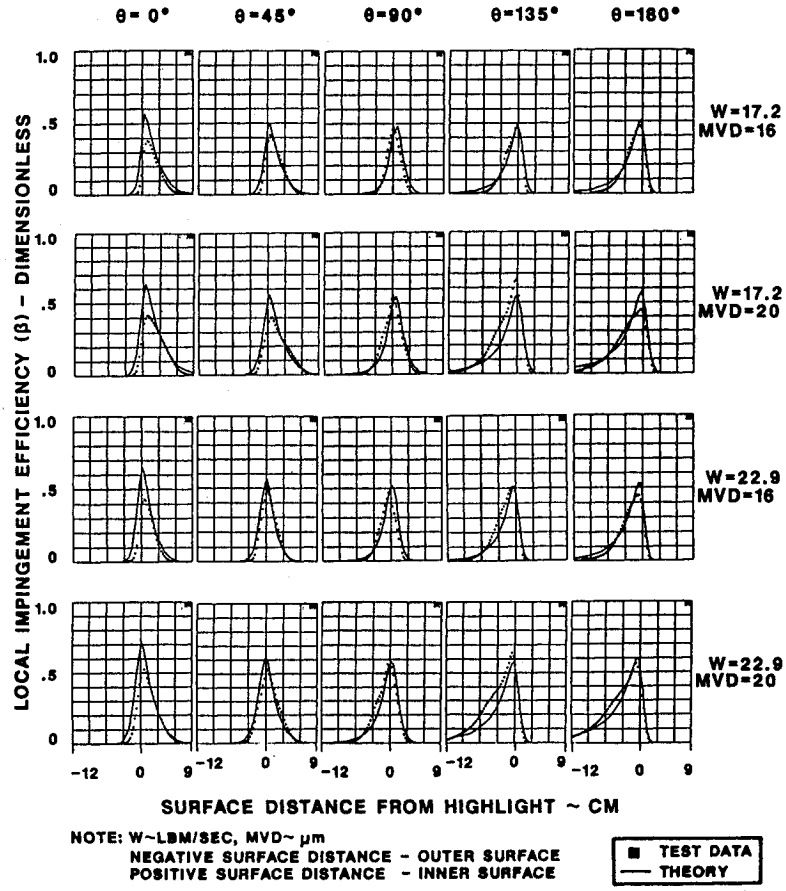

Fig. 10 Impingement efficiency—test and theory for axisymmetric inlet, $\alpha = 15$ deg, $V_\infty = 165$ mph.

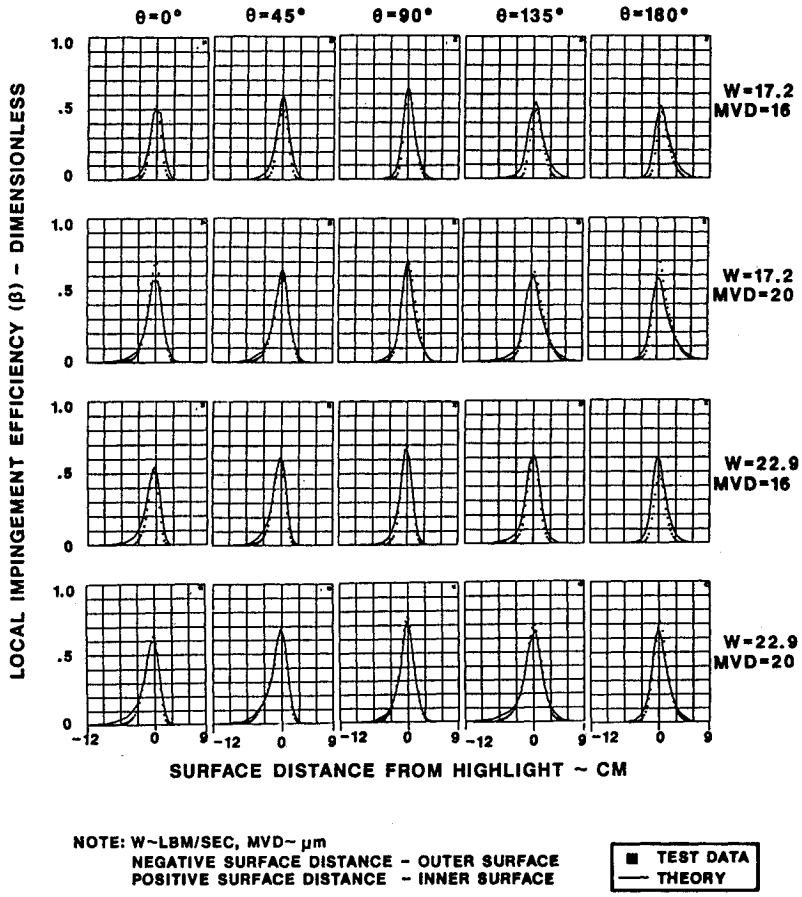

Fig. 11 Impingement efficiency—test and theory for 737-300 inlet, $\alpha = 0$ deg, $V_\infty = 165$ mph.

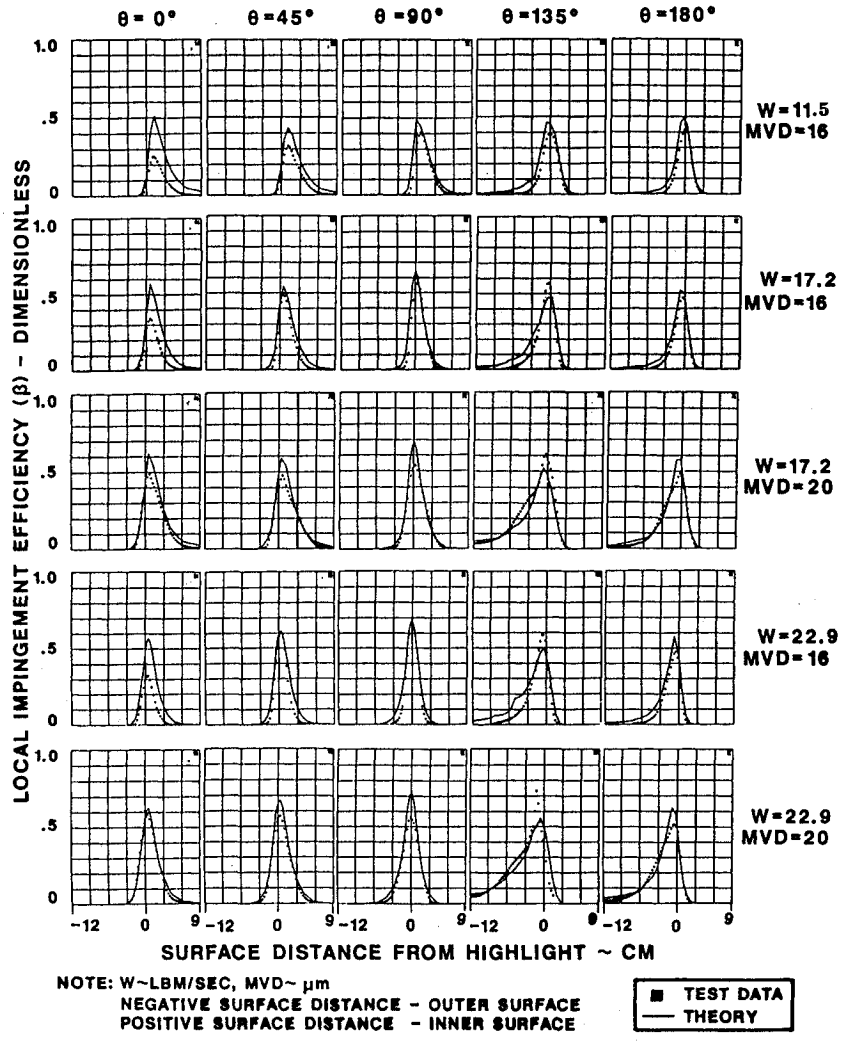

Fig. 12 Impingement efficiency—test and theory for 737-300 inlet, $\alpha = 15$ deg, $V_\infty = 165$ mph.

2) In most cases, if MVD is kept constant, decreasing the inlet suction flow reduces $\bar{\beta}_{max}$ for corresponding inlet surface locations. In addition, the impingement limits and the peak of the $\bar{\beta}$ curve are slightly shifted towards the inner cowl (positive s).

3) For the same inlet mass flow and cloud MVD, the location of $\bar{\beta}_{max}$ shifts from the inner cowl at $\theta = 0$ deg to the highlight at $\theta = 90$ deg and then to the outer cowl at $\theta = 180$ deg.

4) The maximum value of $\bar{\beta}_{max}$ occurs at $\theta = 135$ deg, and the maximum impingement limits are observed at $\theta = 180$ deg.

5) The maximum $\bar{\beta}_{max}$ is approximately 66% and corresponds to MVD = 20 μm, inlet mass flow = 22.9 lbm/s and 17.2 lbm/s, and $\theta = 135$ deg. The minimum $\bar{\beta}_{max}$ is about 38% and corresponds to MVD = 16 μm, inlet mass flow = 17.2 lbm/s, and $\theta = 0$ deg.

Water droplet local impingement efficiency curves for the Boeing 737-300 inlet at $\alpha = 0$ deg for two inlet mass flows, two cloud MVDs, and five different circumferential locations ($\theta = 0$, 45, 90, 135, and 180 deg) are presented in Fig. 11. Figure 12 includes water droplet impingement data for the Boeing 737-300 at $\alpha = 15$ deg for three inlet mass flows, two cloud MVDs, and five different circumferential locations ($\theta = 0$, 45, 90, 135, and 180 deg). Overall, agreement between test and analysis for the Boeing 737-300 inlet is good for both angles of attack. However, at 15 deg angle of attack, for $\theta = 0$ deg, the correlation between analysis and test is poor. The reason for this discrepancy is not clear.

Test results show the following general trends for the 737-300 inlet.

1) For the same inlet mass flow, both $\bar{\beta}_{max}$ and impingement limits decrease with MVD as expected for corresponding θ locations. This is observed for both angles of attack.

2) For the same cloud MVD, decreasing the inlet mass flow results in a decrease in the value of $\bar{\beta}_{max}$ for corresponding θ locations. In addition, both the peak location of the $\bar{\beta}$ curve and the impingement limits are shifted toward the inner cowl. The lower the mass flow, the greater the shift, as shown in Fig. 12. The mass flow effect is the same for both angles of attack.

3) For the same MVD, inlet mass flow, and angle of attack, the only parameter affecting the $\bar{\beta}$ curve is surface location θ. The maximum value of $\bar{\beta}_{max}$ occurs at $\theta = 90$ deg for $\alpha = 0$ deg. For $\alpha = 15$ deg, the maximum value of $\bar{\beta}_{max}$ occurs at $\theta = 90$ and 135 deg depending on inlet mass flow and cloud MVD. For both angles of attack, the extent of impingement limits is maximum at $\theta = 135$ deg.

VI. Summary

Test data have been obtained to provide the data base necessary for validation of trajectory computer codes used for aircraft icing analysis and certification. These data have been used to evaluate results from two trajectory computer codes capable of predicting impingement characteristics of bodies in two- and three-dimensional flows. Water impingement test data for a NACA 65_2015 airfoil, a supercritical airfoil, an axisymmetric inlet, and a Boeing 737-300 inlet have been presented. The experimental and analytical data are found to be in good agreement.

Acknowledgments

This project was funded jointly by the Federal Aviation Adminstration (FAA) and NASA through NASA Research Grant NAG-3-566. The authors would like to thank G. W. Zumwalt, Wichita State University, for his guidance and support throughout the course of this work; J. Riley, FAA, for his encouragement and support; R. J. Shaw and J. Newton, NASA Lewis Research Center, for helping with the tests and supplying the data on droplet distributions; W. Olsen, NASA Lewis Research Center, for his comments and the use of some unpublished material; the NASA Lewis Research Center Icing Research Tunnel personnel for their help with the wind tunnel tests; and R. Nussle, NASA Lewis Research Center, for his technical assistance through the testing.

Thanks are also due to J. Kim, W. Seibel, and M. Smith, Boeing Military Airplanes, Wichita, KS, for providing analytical trajectory data used in this paper; D. T. Dumpert and E. J. Kohman for their help in designing electronic circuitry; and J. Combs for her help in preparing many of the computer plots of the anlaysis and test results.

References

[1]Norment, H. J., "Calculation of Water Drop Trajectories To and About Arbitrary Three-Dimensional Bodies in Potential Airflow," NASA-CR 3291, Aug. 1980.

[2]Bragg, M. B., "An Analytical Approach to Airfoil Icing," AIAA Paper 81-0403, Jan. 1981.

[3]Stock, H. W., "Water Droplet Trajecotry Computation Around an Air Intake," *Zeitschrift für Flugwissenschaften und Weltraumforschung*, Vol. 8, No. 3, May/June 1984, pp. 200–208.

[4]Von Glahn, U. H., Gelder, T. F., and Smyers, W. H., "A Dye-Tracer Technique for Experimentally Obtaining Impingement Characteristics of Arbitrary Bodies and a Method for Determining Droplet Size Distribution," NACA TN-3338, March 1955.

[5]Gelder, T. F., Smyers, W. H., and Von Glahn, U. H., "Experimental Droplet Impingement on Several Two-Dimensional Airfoils with Thickness Ratios of 6 to 16 Percent," NACA TN-3839, Dec. 1956.

[6]Lewis, J. P., and Ruggeri, R. S., "Experimental Droplet Impingement on Four Bodies of Revolution," NACA TN-4092, Dec. 1957.

[7]Gelder, T. F., "Droplet Impingement and Ingestion by Supersonic Nose Inlet in Subsonic Tunnel Conditions," NACA TN-4268, May 1958.

[8]Papadakis, M., Elangovan, R., Freund, G. A., Jr., Breer, M. D., Zumwalt, G. W., and Whitmer, L., "An Experimental Method for Measuring Droplet Impingement Efficiency on Two- and Three-Dimensional Bodies," NASA CR-4257, Nov. 1989.

[9]Kim, J., Vu, S., Craig, N., and Breer, M., "2-D/Axisymmetric Particle Trajectory Computer Program-User Manual," Boeing Document D500-11460-1, Jan. 1990.

[10]Kim, J. J., "Computational Particle Trajectory Analysis on a 3-Dimensional Engine Inlet," AIAA Paper 85-0411, Jan. 1985.

[11]Langmuir, I., and Blodgett, K. B., "A Mathematical Investigation of Water Droplet Trajectories," Army Air Force TR-5418, Feb. 1946.

[12]Breer, M. D., Seibel W., and Lewis-Smith, F. A., "Potential Flow and Data Preparation Programs, Users Manual," Boeing Document D3-9821, July 1976.

[13]Reyhner, T. A., "Transonic Potential Flow Computation About Three-Dimensional Inlets, Ducts, and Bodies," *AIAA Journal*, Vol. 19, No. 9, 1981, pp. 1112–1121.

[14]Reyhner, T. A., "Computation of Transonic Potential Flow About Three-Dimensional Inlets, Ducts, and Body," NASA CR-3514, March 1982.

Recommended Reading from the AIAA Progress in Astronautics and Aeronautics Series . . . AIAA

Thermal Design of Aeroassisted Orbital Transfer Vehicles

H. F. Nelson, editor

Underscoring the importance of sound thermophysical knowledge in spacecraft design, this volume emphasizes effective use of numerical analysis and presents recent advances and current thinking about the design of aeroassisted orbital transfer vehicles (AOTVs). Its 22 chapters cover flow field analysis, trajectories (including impact of atmospheric uncertainties and viscous interaction effects), thermal protection, and surface effects such as temperature-dependent reaction rate expressions for oxygen recombination; surface-ship equations for low-Reynolds-number multicomponent air flow, rate chemistry in flight regimes, and noncatalytic surfaces for metallic heat shields.

***TO ORDER:* Write, Phone or FAX:**
American Institute of Aeronautics and Astronautics,
c/o TASCO, 9 Jay Gould Ct., P.O. Box 753, Waldorf, MD 20604
Phone (301) 645-5643, Dept. 415 ▪ FAX (301) 843-0159

Sales Tax: CA residents, 7%; DC, 6%. For shipping and handling add $4.75 for 1–4 books (call for rates for higher quanties). Orders under $50.00 must be prepaid. Foreign orders must be prepaid. Please allow 4 weeks for delivery. Prices are subject to change without notice. Returns will be accepted within 15 days.

1985 566 pp., illus. Hardback
ISBN 0-915928-94-9
AIAA Members $54.95
Nonmembers $81.95
Order Number V-96